fluids

MDPI

Article

Assessment of Cavitation Erosion Using Combined Numerical and Experimental Approach

Milan Sedlář [1,*], Alois Koutný [2], Tomáš Krátký [1], Martin Komárek [2] and Martin Fulín [1]

[1] Centre of Hydraulic Research, Jana Sigmunda 313, 78349 Lutín, Czech Republic; t.kratky@sigma.cz (T.K.); m.fulin@sigma.cz (M.F.)
[2] SIGMA Research and Development Institute, Jana Sigmunda 313, 78349 Lutín, Czech Republic; koutnyal@centrum.cz (A.K.); m.komarek@sigma.cz (M.K.)
* Correspondence: m.sedlar@sigma.cz

Abstract: This paper aims to numerically assess the cavitation damage of hydrodynamic machines and hydraulic components and its development in time, based on cavitation erosion tests with samples of used materials. The theoretical part of this paper is devoted to the numerical simulation of unsteady multiphase flow by means of computational fluid dynamics (CFD) and to the prediction of the erosive effects of the collapses of cavitation bubbles in the vicinity of solid surfaces. Compressible unsteady Reynolds-averaged Navier–Stokes equations (URANS) are solved together with the Zwart cavitation model. To describe the destructive collapses of vapor bubbles, the modeling of cavitation bubble dynamics along selected streamlines or trajectories is applied. The hybrid Euler–Lagrange approach with one-way coupling and the full Rayleigh–Plesset equation (R–P) are therefore utilized. This paper also describes the experimental apparatus with a rotating disc used to reach genuine hydrodynamic cavitation and conditions similar to those of hydrodynamic machines. The simulations are compared with the obtained experimental data, with good agreement. The proposed methodology enables the application of the results of erosion tests to the real geometry of hydraulic machines and to reliably predict the locations and magnitude of cavitation erosion, so as to select appropriate materials or material treatments for endangered parts.

Keywords: multiphase flow; cavitation erosion; Euler–Lagrange approach; bubble dynamics; CFD; rotating disc apparatus

check for updates

Citation: Sedlář, M.; Koutný, A.; Krátký, T.; Komárek, M.; Fulín, M. Assessment of Cavitation Erosion Using Combined Numerical and Experimental Approach. *Fluids* **2024**, *9*, 259. https://doi.org/10.3390/fluids9110259

Academic Editors: Markus Klein, Priscilla Ribeiro Varges and Faik Hamad

Received: 30 September 2024
Revised: 29 October 2024
Accepted: 29 October 2024
Published: 7 November 2024

Copyright: © 2024 by the authors. Licensee MDPI, Basel, Switzerland. This article is an open access article distributed under the terms and conditions of the Creative Commons Attribution (CC BY) license (https://creativecommons.org/licenses/by/4.0/).

1. Introduction

Cavitation is an important physical phenomenon that can be observed in many spheres of human activity, with both positive and negative impacts. One of the most important consequences of cavitating flow is cavitation erosion. The erosion of solid surfaces by collapsing bubbles is widely used in ultrasonic cleaning, where objects being cleaned are submerged into a liquid in a tank and subjected to an ultrasound field to initiate cavitation. On the other hand, cavitation erosion can be a real problem when operating hydraulic machines, where the loss of material leads to changes in surface properties, decreases in the strength and lifetime of mechanical parts, or serious vibrations of the rotating components. This work aims to address the impacts of cavitation erosion on the performance, efficiency, and reliability of hydrodynamic machinery, so the emphasis is put on hydrodynamic cavitation.

Hydrodynamic cavitation is a specific form of the cavitation phenomenon, with its characteristic features. Though it has already been studied for a long time, especially in connection with the operation of hydrodynamic machines and devices, the assessment of cavitation erosion inside hydrodynamic machinery still represents a challenge for designers, producers, and users. Both experimental methods and numerical simulations are applied in this task.

To carry out short- and long-term tests and to evaluate the cavitation damage and loss of the material, different cavitation erosion facilities are utilized [1,2]. To ensure a rapid cavitation response, the majority of tests resistance to cavitation erosion are carried out with an ultrasonic vibratory apparatus on the basis of the ultrasonic processor, working in tens of kilohertz (typically 20 kHz). It must be pointed out that acoustic cavitation is different from typical hydrodynamic cavitation, and so it is out of the scope of this paper. A much more realistic capturing of the erosion effects of hydrodynamic cavitation is provided by devices based on cavitating liquid jets. Unlike ultrasonic testing, where cavitation bubbles differ only by a little in their size and are excited with a fixed frequency, in the cavitation jet, the distribution of initial cavitation nuclei sizes plays an important role, as does the flow/turbulent structures and unsteady pressure gradients. It is also possible to change the jet parameters (velocity, angle distances, etc.) to reach a wide range of cavitating flow conditions. The application of a special high-speed cavitation tunnel is another possibility for evaluating cavitation damage. The concept and hydraulic design of tunnels can differ significantly, from Venturi tubes to the radial divergent test section. As it will be referenced several times in the next few paragraphs, one special facility should be mentioned in this short survey. This is the cavitation erosion rig used by Franc et al. [3,4] for extensive cavitation pitting and erosion tests. The test section is axisymmetric and made of a converging nozzle 16 mm in diameter followed by a radial divergent channel 2.5 mm in thickness. Under cavitating conditions, a cavity is formed at the sharp edge of the nozzle exit, generating a ring-shaped cavitation erosion area.

Concerning the cavitation erosion in hydrodynamic machines, results most similar to those obtained under conditions inside the rotating parts like impellers or propellers can be obtained in cavitation erosion facilities based on the rotating disc. The working part of the test rig is formed by the chamber with a rotating disc, on which a set of holes, or a set of protruding cavitators, are equally distributed. Either all specimens on the disc can be used to represent a tested material or a set of specimens can be used in the locations of the cavitation erosion generated by the cavity inducers. Usually, the chamber is equipped with radial ribs/baffles suppressing the rotation of the ambient liquid generated by high rotational speeds. Zhang et al. [5] used a disc with six cylindrical rods (10 mm in diameter, 5 mm in height) and six samples. The diameter of the disc was 350 mm, and the test samples were at the radial position of 155 mm. The number of radial baffles was 18. Protruding cavitators (bolt type) were also used by Hong et al. [6] with six specimens at the radial position of 160 mm. Their chamber was equipped with 24 radial ribs. Cheng et al. [7] used four double holes with diameters of 12 mm on a disc with a diameter of 260 mm and four test samples at the radial position of 115 mm. Six baffles equally spaced were welded at the bottom of the chamber. Single-hole cavity inducers with diameters of 10.5 mm were used by Mochizuki et al. [8]. Only two samples on the disc with a diameter of 222 mm and eight stilling ribs were used. Experiments in [6,7] employed water at a temperature of 25 °C. In [5], slurry water in the temperature range of 30–40 °C was used, and in [8], seawater at temperatures of 30, 45, and 60 °C was employed.

Though the experimental methods are essential in the evaluation of the cavitation damage and loss of the material, they can only be used in relatively simple test devices, and the assessment of the cavitation erosion in complex geometries of hydraulic machinery can be unacceptably expensive and time-consuming. In this task, a combination of experimental and numerical methods plays a more and more important role and enables application of the results of erosion tests to the real geometry of hydraulic machines and reliable prediction of the locations and magnitude of cavitation erosion. Though there are a lot of different approaches to assess cavitation erosion numerically, we can consider three main groups of the available methods. The first one is based on the Euler–Euler approach and can be directly used inside the standard CFD tools. Several cavitation erosion assessment methods are generally based on two dominant mechanisms, which result from the material derivative of the potential energy of vapor structures $E_{pot} = (p_0 - p_v)V_v$, where p_0 and p_v are the surrounding and vapor pressures and V_v is the local vapor volume. Based on these two

dominant mechanisms, different researchers select different terms or their combinations, as is summarized in [9]. Nohmi et al. [10] introduced a system of the time-averaged aggressiveness indicators (TAIs) based on the multiplication of temporal derivatives of the volume fraction and the pressure with different natural exponents. Li et al. [11] proposed the intensity function method (IFM) in which the erosion intensity function is based on time derivatives of the local pressure values on the surface and used it in the erosion prediction on the NACA0015 hydrofoil. Dular et al. and Fortes-Patella et al. [12,13] assumed that the relative variation of the pressure difference is an order of magnitude lower than the relative variation of the vapor volume and can be neglected. This assumption is a basis of the gray level method (GLM). So, while IFM focusses on the derivative of pressure, GLM focusses on the derivative of the vapor fraction. A combination of both these methods is usually referenced as the erosive power method (EPM). There are several studies rating the applicability of these methods, e.g., in [14], the GLM and EPM were compared on the Delft twisted hydrofoil [15]. Lei et al. [16] also numerically studied cavitation erosion on the Delft twisted hydrofoil, using the IFM and GLM as well as the time-averaged aggressiveness indicators (TAIs). Concerning the GLM and IFM which apply the threshold values, they found out that for the GLM, the dependence on the threshold is significantly reduced compared to the IFM. To improve the accuracy of the GLM, they used the time-averaged driving pressure as proposed by Melissaris et al. [17]. Melissaris et al. in their work also assumed that the advective term in the material derivative of the vapor volume fraction $D\alpha/Dt$ has a small contribution to the volume change, which allowed them to compute the local impact rate from the partial derivative of the vapor volume fraction $\partial\alpha/\partial t$. To predict cavitation erosion on a NACA65012 hydrofoil with an incidence angle of 6°, Geng et al. [18] applied six erosion risk indicators based on the two dominant mechanisms, which result from the material derivative of the potential energy of vapor structures, including the IFM, GLM, EPM, and Melissaris et al.'s modification. Zhang et al. [19] modified Melissaris et al.'s approach by considering the decay of the shock wave based on the distance from the wall and a limited angle in which the energy is emitted towards the wall. They tested their approach against the experimental data by Franc and applied it practically in combination with the large eddy simulations (LESs) for the numerical prediction of cavitation flow around the NACA0015 hydrofoil. Kevorkijan et al. [20] suggested to define the driving pressure as the pressure values taken directly from steady-state simulations. With the NACA0018-45 hydrofoil as the test case, they showed only a small difference between the results obtained from the driving pressure averaged across one shedding cycle and from the steady-state values. Melissaris et al.'s approach in combination with LES was used in [21] to predict cavitation erosion around the Delft twisted hydrofoil. A practical application of some cavitation erosion criteria on a real hydrodynamic machinery can be found in [22], where the IFM, GLM, and EPM were employed to predict the cavitation risk on the impeller blades of a centrifugal pump and it was found out that the cavitation erosion prediction method based on the rate of pressure change is not suitable for the centrifugal pumps. Another practical application has been shown in [23], where the cavitation erosion intensity on the marine propeller was studied employing the EPM in combination with URANS and detached eddy simulation (DES) turbulence models.

Another approach to the cavitation erosion assessment has been proposed by Dular and Coutier-Delgosha [24] who experimentally and numerically investigated cavitation erosion on a 2D hydrofoil. They suggested the cavitation erosion model based on the hypothesis that the damage of the surface is caused by microjets of collapsing bubbles and that the local velocity of the microjet (if it exceeds the critical threshold) is the critical quantity for the prediction of the erosion potential. The numerical simulations of the two-phase flow were based on a single fluid model where the liquid/vapor mixture is considered as a homogeneous medium whose density varies in the computational domain according to a barotropic state law. Peters et al. [25,26] further developed this model by taking into account the flow properties in the cells in the vicinity of the considered boundary and applied the cavitation modeling based on the volume of fluid (VOF) approach. They

verified their model with experimental tests of sheet cavitation over a NACA0009 hydrofoil, as well as with the experimental data by Franc, and applied it practically for the numerical prediction of cavitation erosion on a ship propeller. The same methodology was used in [27] for the simulation of cavitating flow in an axisymmetric radial divergent channel of 2.5 mm in thickness used by Franc. The cavitation erosion risk in a high-speed gear transmission was investigated in [28], where twelve different cavitation erosion risk indicators (mainly described in [18,25]) were compared.

The second group of cavitation erosion models represents the so-called discrete bubble method (DBM). It combines the simulation of cavitating flow using the Euler-based standard CFD tools with the prediction of the cavitation erosive potential based on the prediction of dynamics of cavitating bubbles using R–P within the Lagrangian approach. In [29], a one-way coupling of Reynolds-averaged Navier–Stokes (RANS) equations and R-P was used to predict the cavitation inception on an axisymmetric headform, but no erosion assessment was performed. Ochiai et al. [30,31] applied this approach to the cavitating flow around the ClarkY hydrofoil and to estimate cavitation erosion, and they evaluated the impact pressure owing to the pressure wave induced by bubble collapses using the methodology derived by Keller and Kolodner [32]. In [33], Ochiai et al. also showed that the bubble nuclei distribution is very important in this approach. In [34], the DBM was compared with the GLM and IFM in the case of flow simulation over a NACA0015 hydrofoil. Sedlář et al. [35] used a similar approach to model unsteady cavitating flow around the NACA2412 hydrofoil, but to evaluate the erosion potential of bubble collapses, they used an integral method estimating the amount of energy available during the collapse causing damage to the surface of the solid material.

The third group of cavitation erosion models extends the second one and includes the methods based on the multiscale approach, in which the two-way transition from vapor structures to cavitating bubbles and back is considered. For the individual bubbles, the momentum equation derived from Newton's second law is applied to track the trajectories. Li et al. [36] used a simplified Rayleigh–Plesset equation, in which all higher-order terms are neglected, to model the growth and collapse of Lagrangian bubbles and the GLM with the time-averaged driving pressure as proposed by Melissaris et al. to assess the cavitation erosion risk on the Delft twisted hydrofoil. Wang et al. [37,38] applied a compressible form of the full Rayleigh–Plesset equation and the erosion potential derived from the evaluation of the pressure pulse in the defined distance from the center of bubble collapse as proposed by Keller and Kolodner. They verified the simulations by the experimental data obtained by Franc in the radially divergent gap and applied their methodology to the Delft twisted hydrofoil. In [39], Wang et al. numerically investigated unsteady cavitating flow around the Delft twisted hydrofoil to analyze the cloud cavitation evolution mechanism and the internal cavity structure. They proposed two different bubble generation mechanisms so as to explain the bubble size distribution spectra in the unsteady cavitating flow. Presented works in this category rely on a correct description of flow and cavitation structures, which is reflected in the application of the large eddy simulations for the turbulence modeling. A different turbulence model was used in [40], where a combination of the two-way transition from vapor structures to the cavitating bubbles and back with the shear stress transport (SST) two-equation turbulence model was applied. The Euler–Lagrange method shows a high potential in accurate simulations of cavitating flow characteristics. A comprehensive review was performed by Ji et al. [41], who also add some outlook of the tasks and perspectives of this group of cavitation models.

The last category of cavitation erosion models includes the methods which cannot be directly included in the above-mentioned groups, e.g., methods based on the analysis of flow dynamics and the impact load spectra. Mihatsch et al. [42,43] introduced a methodology based on the simulation, which takes into account the compressibility of both phases and resolves collapse-induced pressure waves. To detect collapse events in the fluid domain and quantify their spectrum, they introduced a collapse detection algorithm based on vanishing vapor content and the divergence of velocity. The collapse strength

is characterized by its maximum (negative) divergence and its maximum pressure. The methodology has been verified by the experimental data obtained by Franc in the radially divergent gap. The same collapse detection algorithm has been used in [44] to compare the streamwise distribution of flow aggressiveness with the experimental data by Dular and Coutier-Delgosha [24]. This methodology was used in [45] to assess the aggressiveness of the collapse events in the leading-edge cavitation formed over a modified NACA0009 hydrofoil. Trummler et al. [46] modeled cavitation erosion due to a cavitating jet and used Mihatsch et al.'s approach, as well as two other indicators based on the maximum wall pressure and the so-called numerical pit equivalents (NPEs), based on recording in time the pressure exceeding the selected threshold value.

Even though a lot of work has already been devoted to the appropriate methods able to assess the hydrodynamic cavitation, the numerical modeling of cavitation erosion still represents a challenge for researchers as well as the developers of CFD tools. The methods, based on the full Euler–Euler approach, and the material derivative of the potential energy of vapor structures are very sensitive to both the time and space resolution. The collapse detection algorithm, based on vanishing vapor content and the divergence of velocity in the mentioned last category, is sensitive to the time and space resolution as well. The DBMs combined with the evaluation of the impact pressure owing to the pressure wave induced by the bubble collapse are sensitive to the evaluation of the bubble radius derivatives, depending on the time steps which can reach, during the bubble collapse, values several orders lower (cca 10^{-10}–10^{-12}) than those for the CFD simulation. The DBMs also lack the description of large bubble formations like cavitation bubble clouds. This problem is addressed by the cavitation models from the previously mentioned third group, but the detailed description of the bubble–bubble interactions and the coherent collapse, when the shock wave forms near the surface of the cloud and propagates inward and passes the bubbles in the cloud and causes them to collapse [47], is still not provided. The cavitating flow behavior is also very sensitive to the nuclei content. Nevertheless, in commonly used CFD applications the dependence of cavitation on the nuclei content is typically neglected or highly simplified (usually only one size of the initial nuclei radius is considered).

The presented study of the cavitation erosion modeling is basically based on the DBMs, but the evaluation of the erosion risk is based on an integral criterion less sensitive to the bubble radius derivatives. The aim is to provide a robust and relatively simple methodology of the cavitation erosion assessment and to verify it by experimental data measured in the cavitation erosion rig based on the rotating disc. Against the above background the paper is composed as follows. Section 2 presents in detail the methods used within the CFD analysis and the R-P dynamic model and shows the study case and a brief description of the experimental stand and measurement conditions. The results of simulations are presented in detail in the third section, including the comparisons with experimental data. In the Discussion, the results are summarized with some practical applications.

2. Materials and Methods

2.1. Numerical Methods

The CFD part of the computational procedure is based on the ANSYS CFX software package (ANSYS 2020 R2, [48]) which is applied to solve the transport equations including the compressibility and thermal effect.

Calculations are based on unsteady Reynolds-averaged Navier–Stokes equations:

$$\frac{\partial \rho}{\partial t} + \frac{\partial \rho U_i}{\partial x_i} = 0 \tag{1}$$

$$\frac{\partial \rho U_i}{\partial t} + \frac{\partial \left(\rho U_i U_j\right)}{\partial x_j} = -\frac{\partial P}{\partial x_i} + \frac{\partial}{\partial x_j}\left(\tau_{ji}\right) + S_{M,i} \tag{2}$$

where

$$\tau_{ij} = (\mu + \mu_t)\left(\frac{\partial U_i}{\partial x_j} + \frac{\partial U_j}{\partial x_i} - \frac{2}{3}\frac{\partial U_k}{\partial x_k}\delta_{ij}\right) \tag{3}$$

is the viscous stress tensor, U_i are the Reynolds-averaged velocity components in the three-dimensional Cartesian coordinate system, ρ is the fluid density, P is the Reynolds-averaged static pressure, μ is the dynamic viscosity, μ_t is the turbulent viscosity obtained from the turbulence model, and S_M is the general momentum source term. The conservation equation of temperature for the mixture phase is based on the mixture total energy conservation equation:

$$\frac{\partial \rho H}{\partial t} + \frac{\partial (\rho U_j H)}{\partial x_j} = \frac{\partial P}{\partial t} + \frac{\partial}{\partial x_j}\left[\lambda \frac{\partial T}{\partial x_j}\right] + \frac{\partial}{\partial x_j}\left[\tau_{ji} U_i\right] + S_E \tag{4}$$

where H is the total enthalpy, λ is the thermal conductivity, T is the temperature, and S_E is the general heat source term. The real physical properties of both the water and water vapor properties are described by the real gas property (RGP) table, as shown in [49]. The undissolved air in the water is treated as the ideal gas.

To correctly capture the unsteady flow phenomena, the scale-adaptive simulation (SAS) turbulence model (Menter and Egorov [50]) is used, providing the scale-resolving simulation of vortical structures. The SST-SAS turbulence model is based on the widely used SST turbulence model which blends the standard k-ε and k-ω models using two blending functions (F1 and F2) which are dependent on the dimensionless wall distance. The SST-SAS turbulence model can be described by the following governing equations:

$$\frac{\partial \rho k}{\partial t} + \frac{\partial \left(\rho U_j k\right)}{\partial x_j} = \frac{\partial}{\partial x_j}\left[\left(\mu + \frac{\mu_t}{\sigma_{k3}}\right)\frac{\partial k}{\partial x_j}\right] + P_k - \beta^* \rho k \omega \tag{5}$$

$$\frac{\partial \rho \omega}{\partial t} + \frac{\partial \left(\rho U_j \omega\right)}{\partial x_j} = \frac{\partial}{\partial x_j}\left[\left(\mu + \frac{\mu_t}{\sigma_{\omega 3}}\right)\frac{\partial \omega}{\partial x_j}\right] + \frac{\gamma \rho}{\mu_t} P_k - \beta_3 \rho \omega^2 + (1 - F1)\frac{2\rho}{\sigma_{\omega 2}\omega}\frac{\partial k}{\partial x_j}\frac{\partial \omega}{\partial x_j} + Q_{SAS} \tag{6}$$

where

$$P_k = \mu_t\left(\frac{\partial U_i}{\partial x_j} + \frac{\partial U_j}{\partial x_i}\right)\frac{\partial U_i}{\partial x_j} - \frac{2}{3}\frac{\partial U_k}{\partial x_k}\left(3\mu_t \frac{\partial U_k}{\partial x_k} + \rho k\right) \tag{7}$$

is the turbulence production term, k is the turbulent kinetic energy and ω is the turbulent frequency. The turbulent viscosity is described in the following formula:

$$\mu_t = \frac{\rho a_1 k}{\max(a_1 \omega, SF2)} \tag{8}$$

where S is the strain rate:

$$S = \sqrt{2 S_{ij} S_{ij}}, \quad S_{ij} = \frac{1}{2}\left(\frac{\partial U_i}{\partial x_j} + \frac{\partial U_j}{\partial x_i}\right). \tag{9}$$

The source term Q_{SAS} on the right-hand side of Equation (6) represents the additional term comparing to the SST turbulence model and can be expressed as

$$Q_{SAS} = max\left[\rho \varsigma_2 \kappa S^2 \left(\frac{L}{L_{vk}}\right)^2 - C\frac{2\rho k}{\sigma_\Phi} G_{\omega k}, 0\right], \quad G_{\omega k} = max\left(\frac{1}{\omega^2}\frac{\partial \omega}{\partial x_j}\frac{\partial \omega}{\partial x_j}, \frac{1}{k^2}\frac{\partial k}{\partial x_j}\frac{\partial k}{\partial x_j}\right) \tag{10}$$

where L is the turbulence length scale and L_{vk} is the von Karman length scale given by

$$L_{vk} = max\left[\frac{\kappa S}{|U''|}, C_S\sqrt{\frac{\kappa\zeta_2}{\left(\frac{\beta}{c_\mu}-\alpha\right)}}.\Delta_{cell}\right],\ L = \frac{\sqrt{k}}{c_\mu^{0.25}\,\omega},\ |U''| = \sqrt{\sum_i\left(\frac{\partial^2 U_i}{\partial x_j \partial x_j}\right)^2} \tag{11}$$

where κ is the von Karman constant. The limiter of the von Karman length scale is proportional to the mesh cell size, which is calculated as the cubic root of the control volume Ω_{CV}. With this definition of the limiter, the SST-SAS model provides nearly the same energy spectrum as the Smagorinsky LES model. During the last two decades, the SST-SAS model became a highly valued turbulence model for scale-resolving simulations. It is very robust and enables solving problems with high adverse pressure gradients and separated and swirling flows. More details of Menter's SST and SAS models, including a definition and discussion of the blending functions and all used constants (a, C, β, σ, γ, ζ), can be found in [50,51].

The multiphase flows inside the CFD part employ the VOF method, solving the transport equation for the void volume fraction (Hirt and Nichols [52]):

$$\frac{\partial(\rho_v \alpha_v)}{\partial t} + \frac{\partial \rho_v \alpha_v u_i}{\partial x_i} = m^+ - m^- \tag{12}$$

where m^+ and m^- are the rates of the evaporation and condensation of vapor derived based on the Zwart–Gerber–Belamri cavitation model [53], in which the empirical (evaporation and condensation) coefficients have been fitted for a temperature higher than the standard room temperatures:

$$m^+ = F_{vap}\frac{3\alpha_{nuc}(1-\alpha_v)\rho_v}{R}\sqrt{\frac{2}{3}\frac{p_v - p}{\rho_l}},\ p < p_v \tag{13}$$

$$m^- = F_{cond}\frac{3\alpha_v \rho_v}{R}\sqrt{\frac{2}{3}\frac{p - p_v}{\rho_l}},\ p > p_v \tag{14}$$

where R is the bubble radius, p is the pressure, p_v is the equilibrium vapor pressure, indexes v and l represent the vapor/void and liquid phase. α is the volume fraction and F_{vap} and F_{cond} are the empirical evaporation and condensation coefficients and will be discussed later on. The source terms in Equations (12)–(14) have been obtained from the R-P equation, in which all higher-order terms are neglected. Such a simplification does not allow prediction of the rebounds of the cavitation bubbles or the position and energy of the bubble collapses.

To describe the destructive collapses of vapor bubbles, the modeling of cavitation bubble dynamics along selected streamlines (or trajectories), coming through the regions with the pressure drops, is applied. In this model the full R-P equation is employed as described in Zima et al. [54]:

$$R\frac{D^2R}{Dt^2} + \frac{3}{2}\left(\frac{DR}{Dt}\right)^2 + \frac{2\sigma}{\rho_L R}\left[1 - \left(\frac{R_0}{R}\right)^{3\kappa-1}\right] + \frac{4\nu_e}{R}\frac{DR}{Dt} = \frac{p_v - p_0}{\rho_l}\left[1 - \left(\frac{R_0}{R}\right)^{3\kappa}\right] + \frac{p_0 - p}{\rho_l} + \frac{R}{\rho_l c_l}\frac{D}{Dt}(p_g - p). \tag{15}$$

Here, p_0 is the liquid ambient pressure in the undisturbed initial condition, p_g is the pressure of the gas mixture inside the bubble, c_l is the sound velocity of the liquid, σ is the surface tension of the liquid for the gas mixture inside the bubble. ν_e represents the "effective" viscosity, which is taken as an empirical multiple of the kinematic viscosity (typically 10–50 ν) to account for damping mechanisms in the form of viscous dissipation [55]. The last term on the right-hand side of Equation (15) takes into account the compressibility of the fluid during the bubble collapse. So that the bubble rebounds could be modeled, the bubble must contain some amount of a non-condensable gas. Therefore, it is assumed that

the bubble interior contains a mixture of non-condensable gases with the polytropic index κ obeying the following laws:

$$p_g \, R^{3\kappa} = p_{g0} \, {R_0}^{3\kappa}, \qquad p_{g0} = p_0 - p_v + 2\sigma/R_0. \tag{16}$$

Based on the thermodynamic assumptions, the gas inside the bubbles is assumed to behave isothermally, i.e., $\kappa = 1$, during the bubble growth and to behave adiabatically, i.e., $\kappa = 1.4$, during the bubble collapse.

Bubble–bubble interactions are neglected. Bubbles are assumed to be spherical, but the bubble breakup model described in Delale et al. [56] and Zima and Sedlář [57] is implemented, considering the deviations from the spherical symmetry caused by perturbations in the surrounding liquid and inside the bubble. When neglecting the effect of the wall, the bubble surface is perturbed in the following form:

$$r(\varphi, \theta, t) = R(t) + a_n(t) Y_n^l(\varphi, \theta) \tag{17}$$

where $Y_n^l(\varphi, \theta)$ is the spherical harmonic function with mode $n > 1$ and $a_n(t)$ is the amplitude of the perturbations. From the linear Rayleigh–Taylor analysis of Equation (15) while neglecting the role of viscosity, it is possible to determine the most unstable perturbation mode n_m and its amplitude growth with the following criterion for the breakup:

$$a_n\left(t_{b-up}\right) = 0.26 R_{b-up}. \tag{18}$$

Resulting fragments form n_m equivalent bubbles with the radius

$$R_f = R_{b-up} / n_m^{1/3}. \tag{19}$$

After the breakup of the parental bubble, dynamics of the fragmental bubbles obey the following equation:

$$R\frac{D^2R}{Dt^2} + \frac{2\sigma}{\rho_L R}\left[1 - \left(\frac{R_f}{R_{b-up}}\right)^{3\kappa}\left(\frac{R_0}{R}\right)^{3\kappa-1}\right] + \frac{3}{2}\left(\frac{DR}{Dt}\right)^2 + \frac{4\nu_e}{R}\frac{DR}{Dt}$$

$$= \frac{R}{\rho_l c_l}\frac{D}{Dt}(p_g - p) + \frac{p_0 - p}{\rho_l} + \frac{p_v - p_0}{\rho_l}\left[1 - \left(\frac{R_f}{R_{b-up}}\right)^{3\kappa}\left(\frac{R_0}{R}\right)^{3\kappa}\right]. \tag{20}$$

Under the hydrodynamic cavitation conditions, the first two collapses are usually the most important ones and, consequently, the number of rebounds is limited to two.

It is assumed that the main contribution to the erosion of solid materials arises from the mechanical effects of the collapsing bubble near the solid surface. These effects are represented by the impact of a spherical shock wave propagated from the center of the collapsing bubble. The erosion potential of this shock wave is estimated from the energy dissipated during this collapse [54]. The energy dissipated during the i-th collapse of the bubble $E_{i,i+1}$ is obtained as the difference between the work performed by the pressure inside the bubble p_B against the ambient liquid pressure p to expand the bubble from the minimum radius $R_{min,i}$ to the maximum radius $R_{max,i}$ during the i-th growth and the same work during the $(i + 1)$-th bubble growth:

$$E_{i,i+1} = W_{growth}|_{R_{min,i}}^{R_{max,i}} - W_{growth}|_{R_{min,i+1}}^{R_{max,i+1}} \tag{21}$$

$$W_{growth}|_{R_{min}}^{R_{max}} = \int_{R_{min}}^{R_{max}} 4\pi R^2 (p - p_B) dR. \tag{22}$$

Only a part of the shock wave energy dissipated during the collapse is supposed to be emitted towards the solid surface, and the erosive effect depends on the ratio between the maximum radius $R_{max,i}$ and the local distance of the bubble center from the wall d_w. In this

study one quarter of the shock wave energy dissipated during the collapse is supposed to be emitted towards the wall, which corresponds to the solid angle of π (or plane angle of 120°). In the literature, there are different corrections of the impact pressure (or energy) based on the normalized bubble–wall distance $\gamma = d_w/R_{max}$. Wang et al. [37,38] and Peters and Moctar [40] used two different rather complex functions for the first and the second collapses of the bubble. Generally, a simple relation of the pressure decay can be written as follows:

$$\frac{p_1}{p_0} = \left(\frac{r_1}{r_0}\right)^{n_d} \tag{23}$$

where r_i is the radius of the acoustic wave, p_i is the pressure at the wave's considered radius, and n_d is the pressure decay slope. Vogel et al. [58] and Peters and Moctar [40] report the decay slope in the range from -1 to -2.3, changing with the distance. Zhang et al. [19] therefore define the so-called hydrodynamic efficiency of the potential power density to be one for $\gamma < 1$ and employ the decay slopes of -1.3 for $1 < \gamma < 2$ and -2.2 for $\gamma > 2$.

Based on the above considerations, in this study the evaluation of the collapse erosion energy E_E is described by the following function:

$$E_E = \frac{1}{4}\Phi\left(\frac{R_{max,i}}{d_w}\right) PE_{i,i+1}. \tag{24}$$

Function Φ reaches the value of 1 for the distance ratio equal or greater than 1 and decreases with the second negative power for the distance ratio $1/\gamma$ less than 1. The function P represents a probability of the event in the framework of the unsteady flow as the flow is split into several phases, which are assigned with their probability of occurrence in time.

It is considered that the water running through the hydraulic machinery parts contains a known number of microbubbles of the known size distribution, filled with the vapor and a non-condensable gas. The number and size of the initial cavitation nuclei can be predicted experimentally [54] or taken from the literature. The simplest general description of the nuclei distribution uses the bubble number density distribution function N(R) [m^{-4}], which shows the number of bubbles of the given size range in the unit volume. It is usually considered to be proportional to the negative power of the bubble radius. Farrell [29] considered the negative power in the range from -3 to -4. Ochiai et al. [33] considered the negative power in the range from -3 to -4 and, in the end, they used the power of -3.5 for their simulations. They also excluded the bubbles smaller than 10 μm from their considerations as they did not cause the impulsive forces to exceed the selected threshold. Wang [59] used the negative power of -4 as the typical distribution of nuclei in the range from 10 μm to 200 μm. Kato et al. [60] suggested (based on their measurements) higher negative power of about -5. To capture the peak in the nuclei population, which is often observed at a small bubble radius, Liu and Brennen [61] used a non-trivial density distribution function based on the combination of exponential and logarithmic functions. Peters and Moctar [40] used (based on the measurements by Reuter et al. [62]) the piecewise continuous nuclei distribution, which combines the quadratic polynomial for the nuclei radius under 2.2 μm, and the sum of an exponential decay and a Gaussian distribution for the larger nuclei. A slightly simpler distribution is described in Zhu and Wang [63] where the considered number density distribution is proportional to the negative power of -4.36 for the bubble radius larger than the critical value R_0 and constant for all smaller bubble radii.

The nuclei number density distribution used in this paper comes from the measurements by the acoustic bubble spectrometer (ABS) [57,64] based on the methodology described in Chahine and Kalumuck [65]. Figure 1 shows the nuclei distribution derived from the data measured by the ABS in the SIGMA R&D Institute in the range from 15 to 150 μm. These data obey the negative power of about -3 very well and so they have been extended with this power up to the upper radius of 200 μm. For the radii smaller than 10 μm, a constant distribution has been selected. The proposed nuclei number den-

sity distribution is compared with the experimental data obtained in [65] and theoretical distributions in [33,40,59,63].

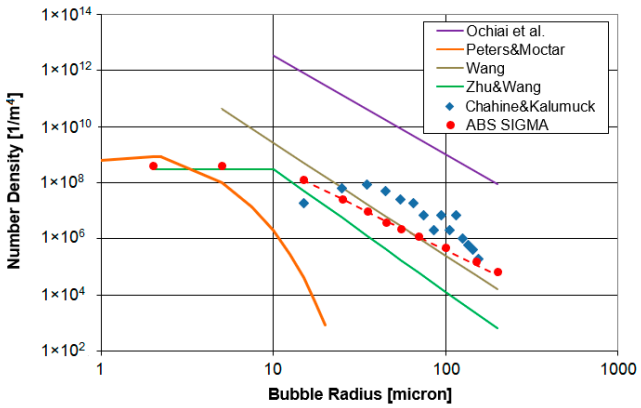


Figure 1. Bubble number density distribution measured by ABS (red dots) in comparison with other sources [33,40,59,63,65].

The values of E_E are calculated for each bubble collapse, summed up for all bubbles along each streamline (or trajectory, as will be discussed in the next paragraph) and expressed as the power per unit area e_{EP} (erosion potential). It should be emphasized that e_{EP} is a proportional value without a straight physical utilization. To define a function of the material loss in time $M_L(t,T_r,v_r)$ for the appropriate temperature and velocity levels T_r, v_r, the values of e_{EP} must be multiplied by the time-dependent function, derived and calibrated on the basis of available experimental data.

For a steady-state or quasi-steady cavitating flow, Equations (15) and (20) are solved along a pre-defined set of streamlines. For highly unsteady flows, the integration should be performed along the trajectories, which correctly describe the cavitation bubble movement inside the flow field. The trajectories are updated at each global time step of the macroscopic (URANS) analysis. The reason why both the streamlines and trajectories are considered is straightforward because the ANSYS CFX software does not enable the Lagrange tracking of the cavitation bubbles inside the multiphase flow and so the real Lagrange tracking should be performed using the user-defined routines, which read the CFX transient result files. This approach requires a large disk space to share the data and makes the simulations more time-consuming.

Generally, in each time step single bubbles follow Newton's second law:

$$\frac{d\boldsymbol{x}_b}{dt} = \boldsymbol{U}_b \tag{25}$$

$$m_b \frac{d\boldsymbol{U}_b}{dt} = \sum_a \boldsymbol{F}_a \tag{26}$$

where x_b, U_b, and m_b are the bubble position, velocity, and mass. Functions F_a represent the volume variation force, virtual mass force, pressure gradient force, buoyancy force, and the drag and lift forces acting on the bubble:

$$\boldsymbol{F}_{volume} = 2\pi R^2 \frac{DR}{Dt} \rho_c (\boldsymbol{U} - \boldsymbol{U}_b) \tag{27}$$

$$\boldsymbol{F}_{vm} = \frac{2}{3}\pi R^3 \rho_c \left(\frac{d\boldsymbol{U}}{dt} - \frac{d\boldsymbol{U}_b}{dt} \right) \tag{28}$$

$$\boldsymbol{F}_{pg} = \frac{4}{3}\pi R^3 \rho_c \frac{d\boldsymbol{U}}{dt} \tag{29}$$

$$\boldsymbol{F}_{buoy} = \frac{4}{3}\pi R^3 \boldsymbol{g}(\rho_b - \rho_c) \tag{30}$$

$$\boldsymbol{F}_{drag} = C_d \frac{1}{2}\pi R^2 \rho_c |\boldsymbol{U} - \boldsymbol{U}_b|(\mathbf{U} - \boldsymbol{U}_b) \tag{31}$$

$$\boldsymbol{F}_{lift} = C_l \frac{4}{3}\pi R^3 \rho_c (\boldsymbol{U} - \boldsymbol{U}_b) \times \boldsymbol{\omega} \tag{32}$$

where $\boldsymbol{U}$, $\boldsymbol{g}$,$\boldsymbol{\omega}$ and C_d, C_l are the velocity of homogenous flow field, the gravity vector, the vorticity of flow, and the drag and lift coefficients as described in [38,40]. Index c represents a carrier fluid (the local homogenous mixture of liquid and vapor). Nevertheless, we could also take into account some simplified Lagrange tracking within the ANSYS CFX software using only Equation (25), as has been employed in [35]. If the cavitation model is implemented in the frame of homogenous multiphase flow, it is possible to include the buoyancy force in the governing equations. If the cavitation model is implemented in the framework of inhomogeneous multiphase flow, it is possible to include both the buoyancy and interphase drag forces. Other forces are neglected. In both the cases, the ANSYS software tools are available to track the trajectories at each global time step.

For highly unsteady flows, effects of the coherent collapse of the bubble cloud should be considered. In order to model the effect of shock waves induced by the first bubble collapses on the pressure field in the cavitating cloud, the estimation of the pressure pulse from a spherical bubble collapse can be employed as derived in [32], where the pressure field in the vicinity of the collapsing bubble is approximated as the potential flow induced by the spherical motion of the bubble wall. The pressure p_r at the radial position r from the bubble center during the collapse can be expressed as follows:

$$p_r = p_{0-}\rho_l \left[\frac{f'}{r} + \frac{1}{2}\left(\frac{f^2}{r^4} + \frac{2ff'}{c_l r^3} + \frac{1}{c_l^2}\frac{f'^2}{r^2}\right)\right], \; f\left(t - \frac{r-R}{c_l}\right) = -R^2\frac{DR}{Dt} + \frac{1}{c_l}\left[R^3\frac{D^2R}{Dt^2} + 2R^2\left(\frac{DR}{Dt}\right)^2\right]. \tag{33}$$

The prime denotes the derivative with respect to $t - (r - R)/c_l$ and has to be evaluated numerically. The influence of all pressure pulses with the large magnitudes and very short durations has to be counted up along all flow trajectories at each time step during the internal iterations of the macroscopic flow analysis. This methodology was used in [35].

To compare the results of the cavitation erosion methodology based on Equations (21)–(24), the erosion indicator from the GLM can be evaluated, as introduced in [12,13], assuming that the relative variation of the pressure difference is an order of magnitude lower than the relative variation of the vapor volume:

$$e_{pot} = \frac{DE_{pot}}{Dt} = (p - p_v)\frac{DV_v}{Dt} + V_v\frac{Dp}{Dt}$$

$$e_{pot} = \frac{DE_{pot}}{Dt} \approx (p - p_v)V_{cell}\frac{D\alpha_v}{Dt} \tag{34}$$

$$e_{den} \approx (p - p_v)\frac{D\alpha_v}{Dt} \tag{35}$$

where E_{pot} is the potential energy of a vapor structure and e_{den} is the potential erosion power density [18].

2.2. Case Description and Experimental Facility

The experiment proceeds from the program of international erosion tests [2] utilizing different cavitation erosion tools and different materials. Because hydrodynamic cavitation differs from the cavitation generated by ultrasound devices (both in the timescales and in the character and energy of collapses), the rotating disc apparatus has been employed in the SIGMA Research and Development Institute to reach real hydrodynamic phenomena (Figure 2). The working chamber has two sets of 24 radial baffles (12 of them being shorter) on both sides. The gap between the baffle edge and the disc is 8 mm on both sides. For visualization purposes, a transparent cover was also prepared, having two short baffles

removed for a larger camera window. The disc with the diameter of 275 mm has six cylindrical cavitation holes with the diameter of 6 mm located at the radius of 115 mm (Figure 3). The edge of each hole is ground by 0.5 mm with the grinding angle of 45°. The working liquid is tap water. The water-cooling system is employed to circulate and cool the water inside the chamber. The water input is through the chamber at the shaft, the water output is through the pipe DN26 (located at the bottom, at midspan of the chamber—see Figure 2).

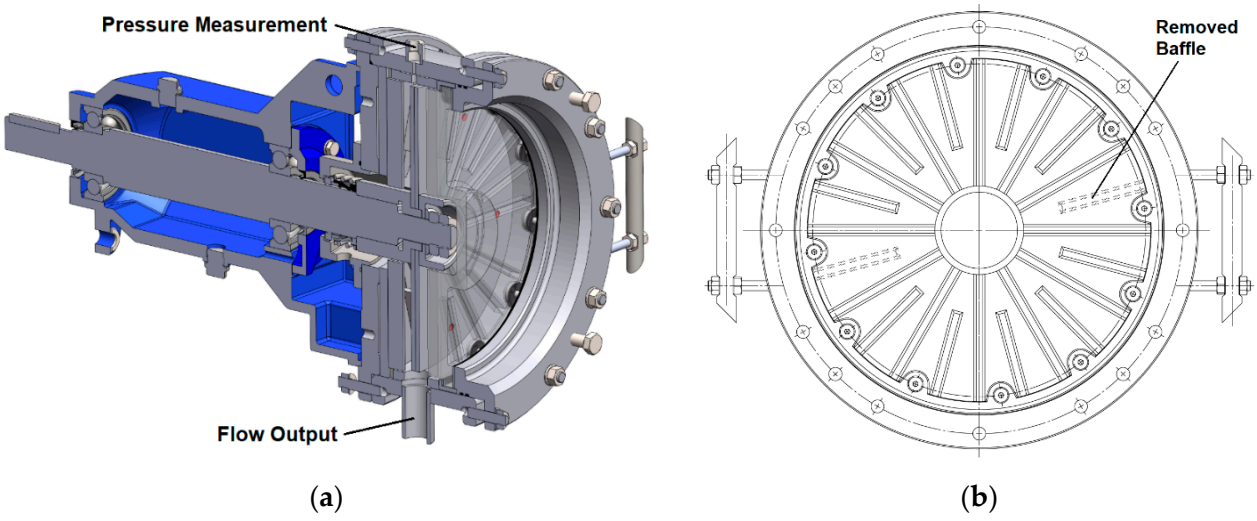


Figure 2. Rotating disc apparatus: (**a**) Section view; (**b**) Cover with transparent wall.

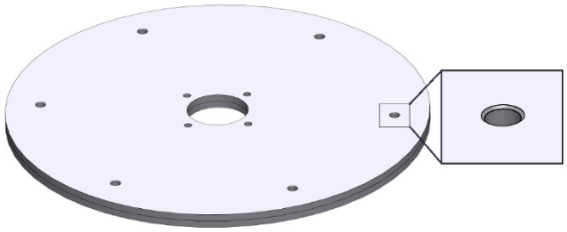


Figure 3. Rotating disc with cavitation holes.

For the large-scale rapid testing, the AlCu4Mg (EN AW 2017A) alloy has been used as the material of the disc. The reference temperature is 40 (±2) °C, the nominal rotational speed is 5000 rpm; a range of rotational speeds and temperatures has been covered. It is not common to state the cavitation number for the rotating disc apparatus, and there is a question about the reference pressure. If we define the cavitation number based on the static pressure measured in the test section (Figure 2) and the peripheral velocity at the center of the cavitation hole, we obtain (for the rotational speed of 5000 rpm) a cavitation number of about 0.035. During the tests, the disc was periodically removed, cleaned, and dried and the material loss was measured with the accuracy of ±0.1 mg. The mass loss was also simply recalculated into the volume loss (as the mass loss divided by the density of the material). Recalculated data have been compared with the optical profilometry output, with a satisfactory agreement. Figure 4 shows the cavitation erosion patterns for three different rotational speeds n.

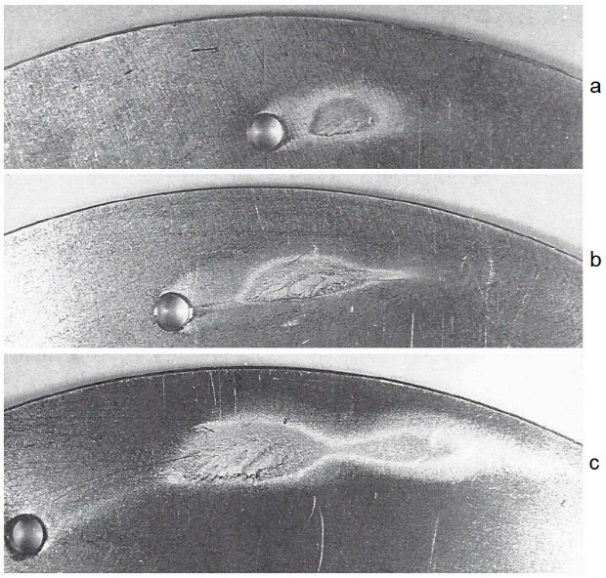


Figure 4. Cavitation erosion patterns after 10 h. (**a**) v_r = 48 m/s, n = 4000 rpm; (**b**) v_r = 60 m/s, n = 5000 rpm; (**c**) v_r = 66 m/s, n = 5500 rpm.

2.3. Computation Set-Up

The CFD simulations have been performed for the working chamber with the full sets of 24 radial baffles on both sides. Complete three-dimensional geometry of the test apparatus (without any symmetry plane) has been used to capture the unsteady flow through the cylindrical cavitation holes (Figure 5).

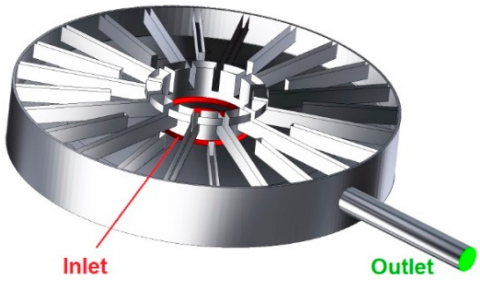
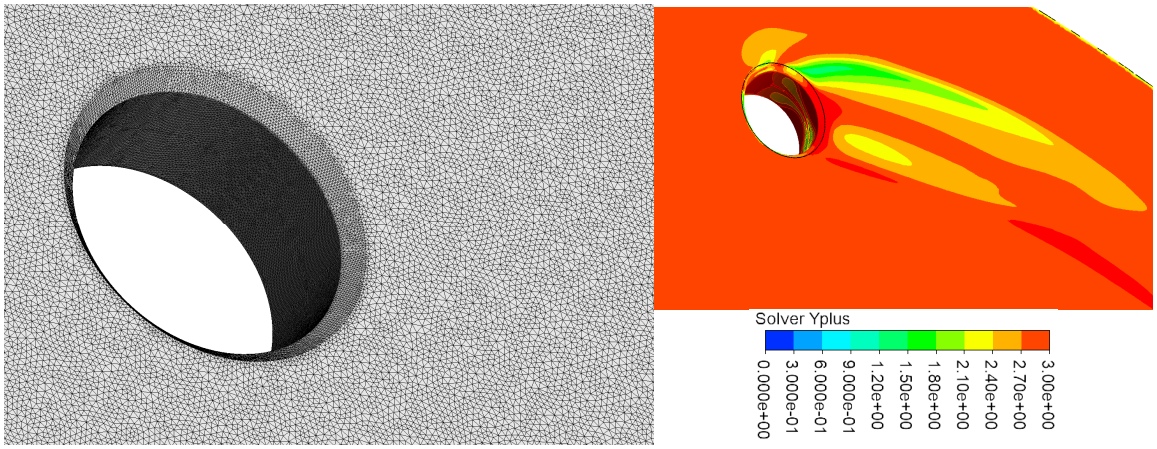


Figure 5. Computational domain with inlet and outlet locations.

Grids of the computational domains have been generated using the ANSYS ICEM CFD software as the multiblock ones and represent about 78 mil. grid nodes. These grids have been created in order to be isotropic enough, as required by the advanced turbulence model used for the simulations, but they should also fulfill the rules for sufficiently low values of y+ at the solid walls (Figure 6). That is why the prism layers are applied in the vicinity of all solid walls. In fact, no typical grid dependence study has been performed, because the topology and local quality of the grid close to the disc surface are much more important in these simulations than the simple number of grid points. Consequently, the meshes are limited in their size just by the request to be able to work within the computer operating memory of 1 TB. For the initial steady-state simulation, the non-dimensional wall-adjacent grid height y+ on the disc does not exceed a value of 3. Concerning the y+ distribution on the stilling baffles, it is very uneven and, in some regions, exceeds the value of 4; still this stator domain is not as important as the rotation disc domain. Still, to cover a wide range of y+ in the whole computational domain, an automatic wall treatment has been applied.



(**a**) (**b**)

Figure 6. Detail of cavitating hole: (**a**) Computational grid; (**b**) Values of y+ at solid walls.

The high-resolution scheme has been used for the momentum equations, while the turbulence numerics is based on the first-order scheme. The time discretization is of the second order and uses the backward Euler scheme. The multiphase flow has been carried out by means of the VOF method. The multiple frames of reference (MFR) capability in which different domains are rotating relative to one another and the fully unsteady model of flow (known usually as the transient rotor–stator or the sliding mesh) inside the entire test apparatus have been used to capture the interactions between the stationary parts inside the chamber and the rotating disc. The time step 1.111×10^{-5} corresponds to the rotor revolution by 0.33°; consequently, one rotor revolution is represented by 1080 time steps. The flow through the chamber has been set to 0.1 L/s. The boundary conditions have been specified as follows: the velocity, turbulent kinetic energy, and its dissipation rate have been prescribed at the inlet according to the flow rate and estimated turbulence intensity. At the outlet the static pressure has been set adjusted so as to reach the measured static pressure of 70 kPa in the position of the pressure probe (Figure 2).

The inlet cavitation nuclei volume fraction has been set (based on the measurements with the acoustic bubble spectrometer) to 1×10^{-4}. Unfortunately, the Zwart–Gerber–Belamri cavitation model allows employment of only one reference initial size of the nuclei. For that reason, the mean nuclei radius has been set to the default value of 2×10^{-6} m, though the measured nuclei radii reach up to 0.2 mm. The empirical cavitation condensation and cavitation vaporization parameters have been modified according to the prescribed nuclei content and reference temperature to F_{vap} = 80 and F_{cond} = 0.002, which gives a good agreement of the cavity sizes with the experiment.

Concerning the modeling of cavitation bubble dynamics, Equations (15) and (20) are solved by the fourth-order Runge–Kutta scheme with the adaptive step size algorithm. When solving the full set of Equations (25)–(32), a semi-implicit scheme is employed as described in [38,40]. In this scheme, the force terms related to the bubble velocity $\boldsymbol{U}_b$ are treated implicitly, while the force terms related to the homogenous field velocity $\boldsymbol{U}$ are treated explicitly.

3. Results

All the results demonstrated in the paper are related to the nominal rotational speed of 5000 rpm. The flow on the disc is periodic as can be seen in Figure 7, showing the pressure fluctuations in the position of the pressure probe. The dominant frequency is 6 f_{shaft}, where f_{shaft} is the shaft frequency. This corresponds to the number of cavitation holes on the disc. The two next most important frequencies are 12 f_{shaft} and 24 f_{shaft}, resulting from the 12 + 12 radial baffles. Concerning the increased pressure amplitude for the shaft frequency itself, it can be related to (only one) flow output from the chamber.

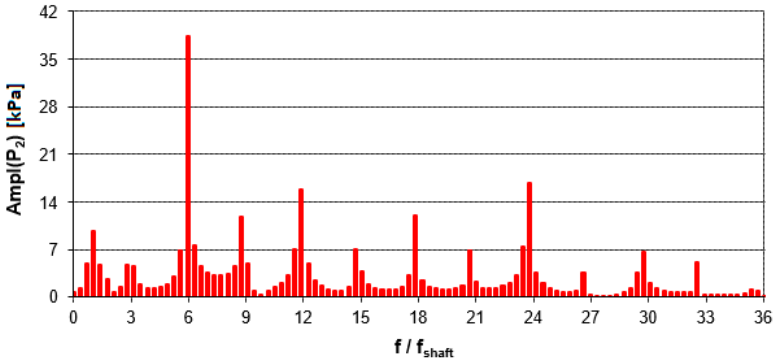


Figure 7. Pressure fluctuations in the position of pressure probe.

For simplicity, only three phases of unsteady periodic flow are presented in Figure 8 showing the shape and size of the cavitation region during the dominant time interval (Figure 8a), as well as the smallest and the largest range of cavitation (Figure 8b,c). The cavitation is generated on the cavitation hole edge and spreads in the streamwise direction. For every phase of flow, a set of streamlines covering the cavitation region is shown in Figure 9. The bubble dynamics of the set of eleven cavitation bubbles with the initial radii from 2 to 200 micrometers has been modeled and the positions of the bubble collapses and their erosion potential e_{EP} have been evaluated. The Lagrangian bubbles (with an undisturbed distribution from Figure 1) are released upstream along the streamlines about three diameters in front of the cavitation hole.

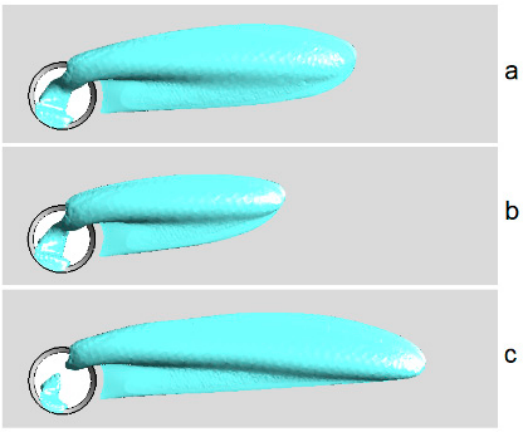


Figure 8. Cavitation regions. n = 5000 rpm. (**a**) Dominant cavitation range; (**b**) Minimum cavitation range; (**c**) Maximum cavitation range. Cavities are represented by iso-surfaces with void volume fraction α_v = 0.5.

As the erosion potential of the first collapses is (in the case of hydrodynamic cavitation with spherical collapses) usually several orders higher than the erosion potential of the other ones, the numerically determined location and magnitude of the first calculated collapses are preferentially presented. For clarity, the positions of the first collapses of bubbles with the initial radius R_0 = 2 μm (brown balls) and R_0 = 200 μm (violet balls) are shown in Figure 9. Green balls represent all collapses of the bubbles in the cavitation hole area, where a very complex swirling and separated flow can be found (Figure 10), resulting in cavitation erosion just behind the hole edge. The position of bubble collapses from Figure 9 against the experimental erosion pattern can be seen in Figure 11.

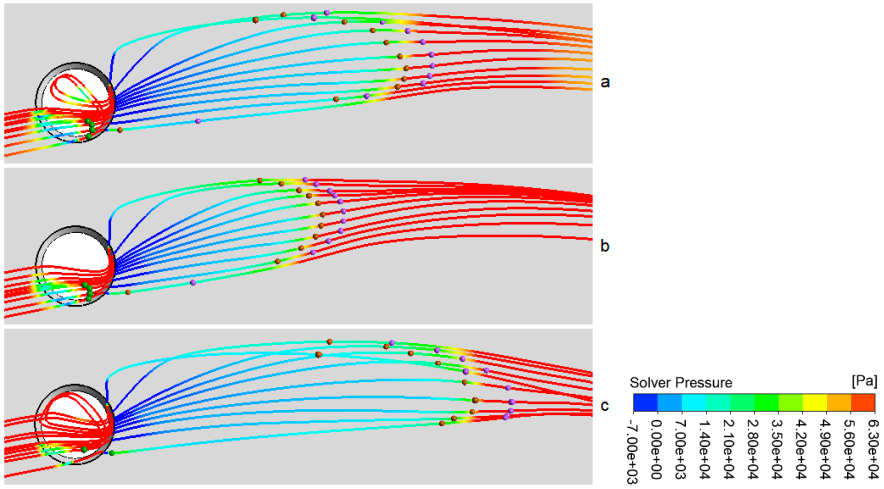


Figure 9. Positions of first bubble collapses. n = 5000 rpm. Brown balls R_0 = 2 µm, violet balls R_0 = 200 µm, green balls represent collapses in cavitation hole area. (**a**) Dominant cavitation range; (**b**) Minimum cavitation range; (**c**) Maximum cavitation range.

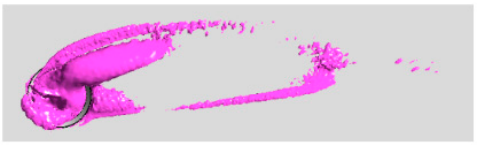


Figure 10. Vortical structures, Q criterion, Q = 6×10^6. n = 5000 rpm. Dominant cavitation range.

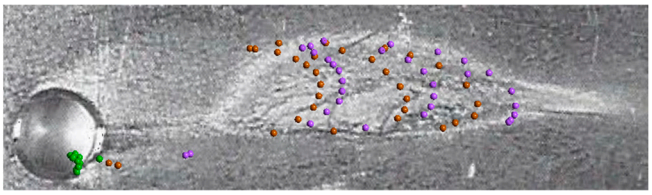


Figure 11. Positions of bubble collapses from Figure 9 against experimental erosion pattern.

Figure 12 shows the dynamics of cavitation bubbles with three different sizes along one streamline. It can be found that the larger the nuclei, the lower is the relative growth. Smaller bubbles collapse sooner than the larger ones. The bubble dynamics can be visible already after the bubble meets the front part of the cavitation hole edge. Collapses from the bubble dynamics can be mainly linked with the green balls from Figure 9. Nevertheless, in a majority of cases, the dominant bubble growth starts behind the rear part of the hole edge, resulting in the collapses represented by the brown and violet balls.

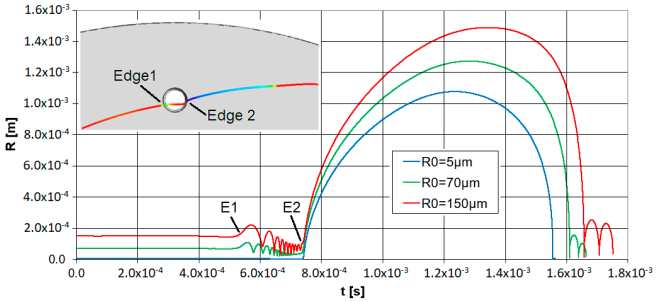


Figure 12. Dynamics of cavitation bubbles with different initial sizes along one streamline from Figure 9a.

The erosion potential along the streamwise path going through the center of the eroded region (magenta line) can be found in the upper graph of Figure 13. The values below the threshold of 0.1 W/m^2 represent the second collapses of the largest cavitation bubbles. When using only three unsteady flow phases, three distinct groups of values are not able to reasonably describe the distribution of the erosion potential along the path. That is why nine unsteady flow phases have been applied in the end to obtain a continuous distribution of the erosion potential, as shown with the magenta dashed line in the upper and middle graphs of Figure 13. The erosion potential along (magenta line) as well as across (green line) the eroded region obtained from the full range of data can be found in the middle and lower graphs of Figure 13. The erosion potential is not uniform in the cross-section (green line); it increases (nearly linearly) with decreasing radial position.

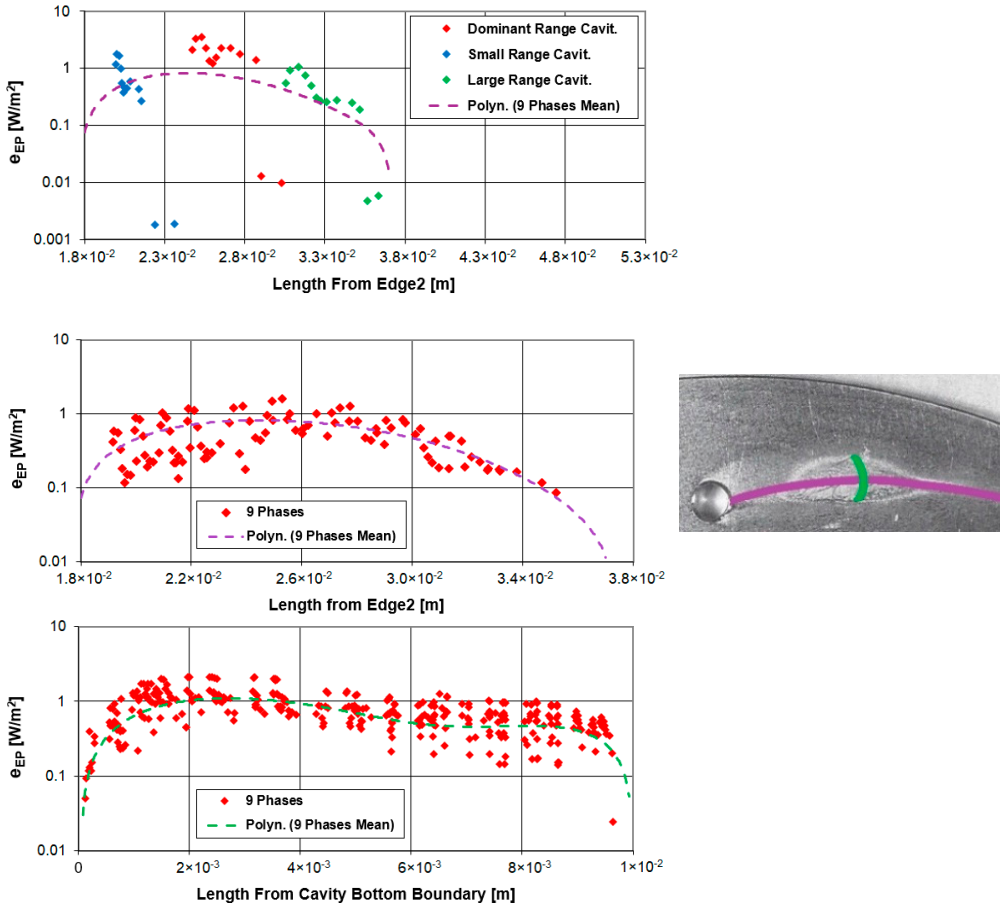
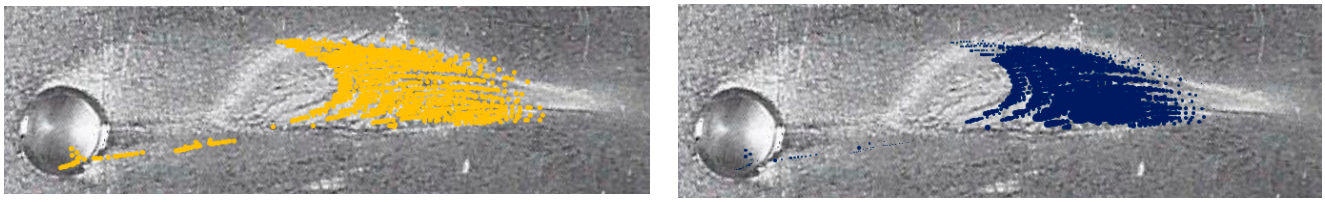


Figure 13. Erosion potential along the magenta path obtained from three phases (**upper** graph) and along the magenta and green paths obtained from nine phases of unsteady periodic flow (**middle** and **lower** graphs).

The projection of the full dataset of bubble collapses on the eroded disc surface can be seen in Figure 14a (yellow dots). In this picture, all the bubble collapses are indicated with the same mark size. Still, this picture does not provide a correct visual perception of the cavitation erosion intensity. Better visual perception can be obtained from Figure 14b (dark blue dots) in which the marks are scaled according to the local erosion potential of bubble collapses. Here, it is assumed that the volume of the material removed by the collapse depends linearly on the erosion potential, so the size of the collapse dot is proportional to the third root of the erosion potential. Figure 15 shows three different views of the normalized depth of eroded area. So as to enable better visual perception, the erosion depth is shown in a scale different from the disc thickness. The individual cavities are simply represented by the small cubes, scaled so as to fit approximately the

pit size distribution measured by the scanning electron microscopy (SEM) and the optical profilometry (Figures 16 and 17).



(**a**) (**b**)

Figure 14. Complete dataset of positions of bubble collapses during one period from Figure 8: (**a**) All collapses share the same mark size; (**b**) Marks are scaled according to local erosion potential.

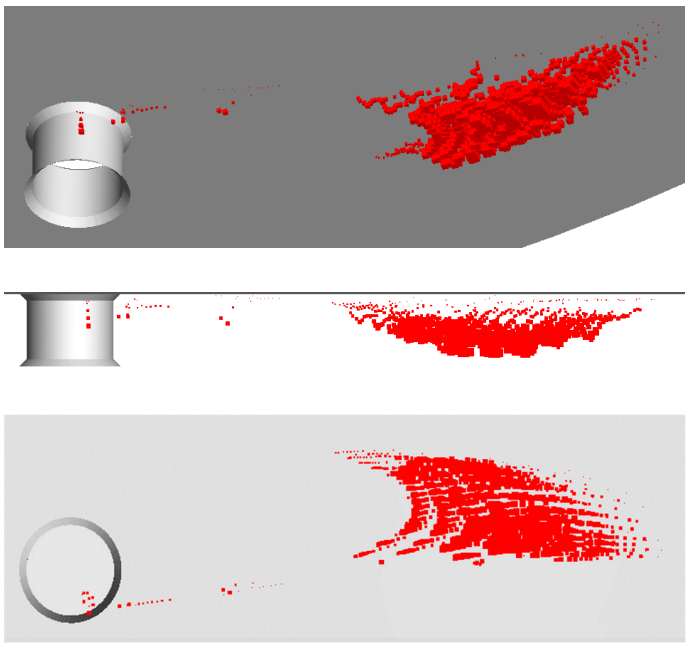
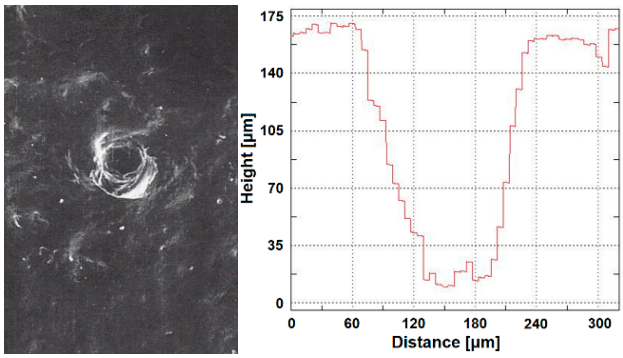


Figure 15. Three-dimensional view (**top**), side view (**middle**) and front view (**bottom**) of eroded area. Marks are scaled according to local erosion potential. Erosion depth is scaled differently from disc thickness.



(**a**) (**b**)

Figure 16. Cavitation damage after the period of plastic deformation: (**a**) SEM image; (**b**) Cavity profile measured by optical profilometry.

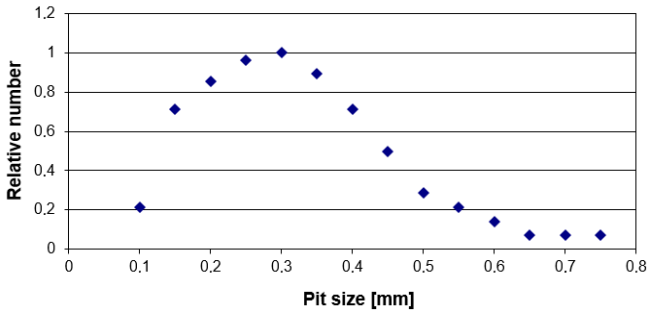


Figure 17. Pit size distribution measured during acceleration period.

Figures 14 and 15 can be compared with the cavitation erosion assessment based on the GLM, as shown in Figure 18. If the threshold of 3×10^7 is adopted (as discussed in [14,16]), the GSM covers nearly the whole area of the cavitation hole edge and the main part of the experimentally eroded area. The width of the erosion region predicted by the GSM is similar to that of the area predicted by the presented bubble dynamic model; it is about 31% shorter along the path going through the center of the eroded region.

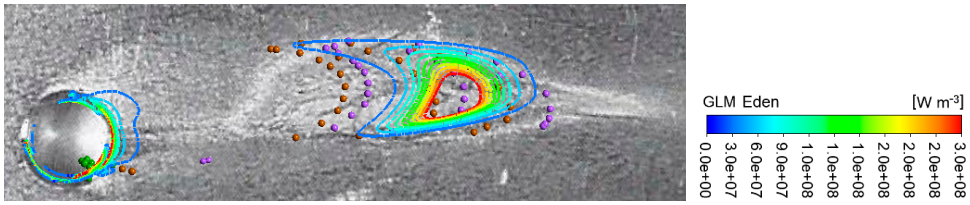


Figure 18. Distribution of cumulative erosion potential evaluated based on GLM. Positions of bubble collapses taken from Figure 9.

4. Discussion

The methodology described and verified in the previous sections should be used for practical applications in hydraulic machines. For these applications, different real-life materials are used for the wetted surfaces of machine working components. For this reason, sets of material samples are used during the cavitation erosion tests in the rotating disc apparatus, mounted behind the cavitation holes. Figure 19 shows one typical specimen shaped as a flat cylinder 25 mm in diameter, made from the 1.4021 (AISI 420) chromium stainless steel, after the 40 h erosion test at the rotational speed of 5000 rpm. The picture indicates that the erosion is more intensive in the lower part of the sample (it increases with the decreasing disc radius).

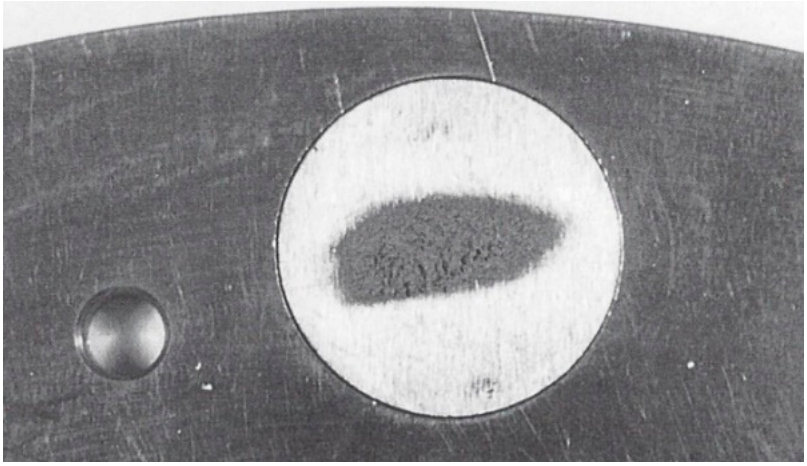
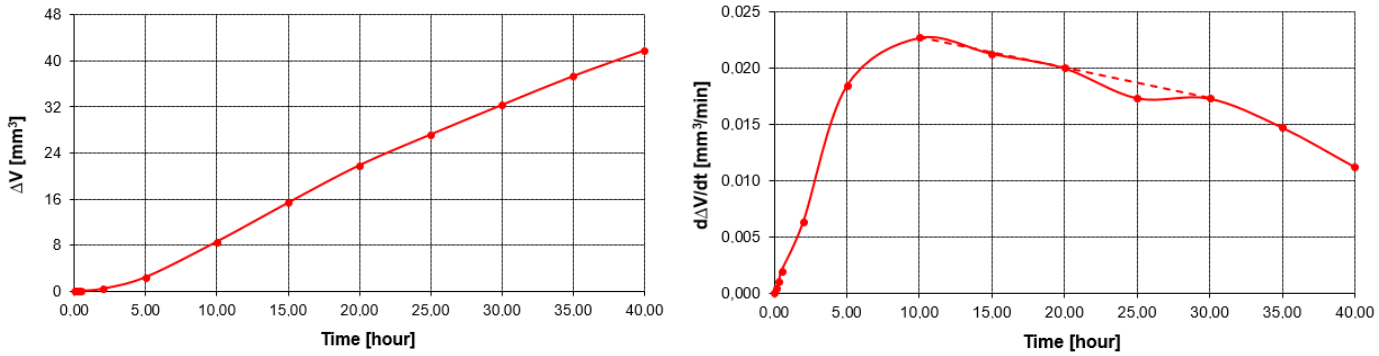


Figure 19. Steel sample after long-term tests.

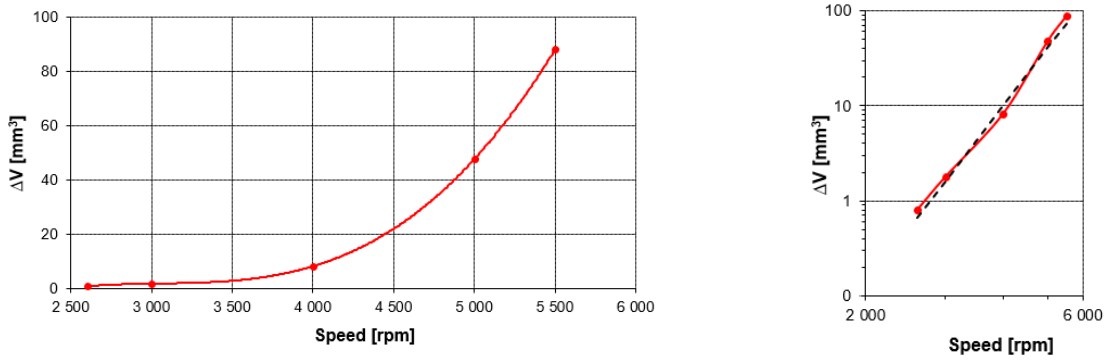
Supposing that the material damage is (nearly) directly proportional to the erosion potential e_{EP}, changes in the material loss in time have been monitored and are ready to create the theoretical function $M_L(t,T_r,v_r)$ available for the subsequent numerical simulations. Figure 20 shows the cumulative volume loss and erosion rate of the steel sample depending on the test duration. The erosion rate has been obtained from the differences of volume losses divided by the time interval duration. The decrease in the erosion rate after reaching the maximum at about 10 h of the test indicates the transition from the acceleration into the deceleration phase of the erosion [66]. During the time span 10–40 h, the erosion rate decreases nearly linearly, as can be seen in Figure 20b.



(**a**) (**b**)

Figure 20. Steel sample during erosion test: (**a**) Cumulative volume loss; (**b**) Erosion rate with nearly linear trend (dashed line).

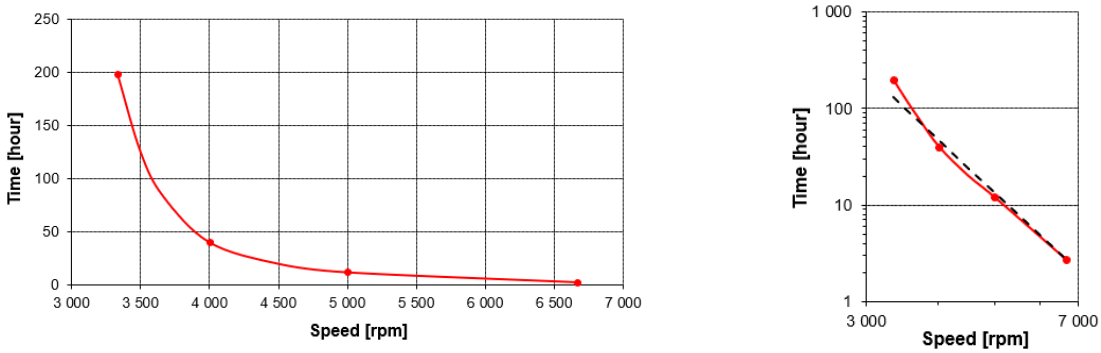
In most applications, the temperature of the water inside the hydraulic machine changes only in very limited range of several degrees, but the rotating speeds could change significantly when the variable speed drives are used. So, it is worth considering scaling of cavitation erosion with the reference velocity. Dular et al. [12] mentioned an enormous influence of the flow velocity on the aggressiveness of cavitation, which can grow with the power-law coefficient of 5–8. That is why the influence of the velocity on the cavitation rate has been tested for both the reference materials: the AlCu4Mg (EN AW 2017A) aluminium alloy and the 1.4021 (AISI 420) chromium stainless steel, so as to obtain the power-law coefficient independent of the material used. The cumulative volume loss after ten hours of operation depending on rotational speed (changing from 2600 rpm to 5500 rpm) is shown in Figure 21 for the aluminium alloy. The approximate power law with the coefficient of 6.3 can be derived from the right-hand graph.



(**a**) (**b**)

Figure 21. Aluminium alloy after 10 h of operation depending on rotational speed: (**a**) Cumulative volume loss; (**b**) Approximate power law (dashed line) with coefficient 6.3.

Because the cumulative volume loss after ten hours of operation for the stainless steel can be quite small for the low rotational speeds (with high relative uncertainty during weighting of samples), a different methodology has been accepted for the 1.4021 steel. The mass loss of 0.1 g has been used as a sufficiently measurable amount, and the time necessary to obtain this mass loss has been evaluated for different rotational speeds. Figure 22 shows the measured test duration based on the rotational speeds (changing from 3300 rpm to 6700 rpm). The approximate power law with the coefficient of −5.6 can be derived from the right-hand graph. Though the methodologies used for different materials differ a little, the power-law coefficient of 6 can be accepted when scaling cavitation erosion with the reference velocity.



(**a**) (**b**)

Figure 22. Erosion of steel sample depending on rotational speed: (**a**) Time necessary to erode steel sample by 0.1 g; (**b**) Approximate power law (dashed line) with coefficient −5.6.

There is also one more topic which should be mentioned in this discussion. It is related to the simulation accuracy when the real trajectories are replaced with the pre-defined set of streamlines or the trajectories are generated just based on Equation (25) and some interphase forces are neglected. The decision is a compromise, which should consider the degree of flow unsteadiness as well as the price for the Lagrange tracking of the cavitation bubbles outside the ANSYS software tools. In this study, the primary calculations are based on the pre-defined set of streamlines for nine unsteady flow phases. To check the relative differences in bubble movement, the set of trajectories has been generated as well and compared with the sets of streamlines. Figure 23 shows such a comparison with streamlines related to the time instant with the dominant cavitation range. In this case of unsteady periodic flow, the differences seem to be acceptable, taking into account saving nearly one half of the computational time.

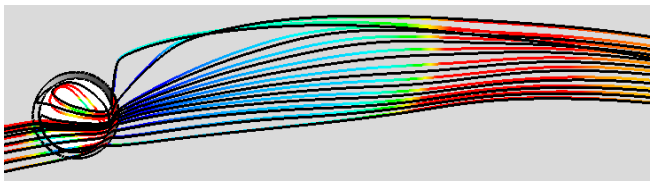


Figure 23. Comparison of generated trajectories (in black) and streamlines related to time instant with dominant cavitation range (rainbow colored).

5. Conclusions

This paper presents a new methodology of the cavitation erosion risk assessment. It aims to address the impacts of cavitation erosion on performance, efficiency, and reliability of hydrodynamic machinery, so the emphasis is put on the hydrodynamic cavitation.

Both the numerical and experimental tools are considered to be used jointly so as to meet the target, at least in the first stage, when the sufficiently accurate calibration data

should be generated in the experimental apparatus. The up-to-date CFD tools have been used for the theoretical predictions and the cavitation erosion stand with the rotating disc has been used to reach genuine hydrodynamic cavitation and conditions similar to those in hydrodynamic machines. The simulations are compared with the obtained experimental data with a good agreement.

Recently, a lot of new metal, composite, or 3D-printed materials have appeared, being used inside hydraulic machines and possibly exposed to cavitation erosion. The samples of these materials can be tested in the cavitation erosion stand. Supposing that the material damage is (nearly) directly proportional to the erosion potential e_{EP}, the changes in the material loss in time can be monitored and used to create the theoretical function $M_L(t,T_r,v_r)$ available for the subsequent numerical simulations. The form of the $M_L(t,\ldots)$ function can depend on the complexity of the data measured in the erosion stand and the available information on the considered real case. The simplest, linear form of the material loss function can be expressed as, based on the newly calculated erosion potential of the case and the mean value of the erosion potential calculated for the experimental configuration,

$$M_{L,case}(t,\ldots) = M_{L,experiment}(t,\ldots)\frac{e_{EP,case}}{e_{EP,exp.stand.mean}} \tag{36}$$

In this way the proposed methodology enables application of the results of the erosion tests to the real geometry of hydraulic machines and to predict reliably the locations and magnitude of cavitation erosion. Following such a prediction, an appropriate material or material treatment can be selected for the endangered parts so as to minimize the negative impacts of cavitation. It is not possible to discuss in detail the potential mitigation strategies of the cavitation erosion risk within this paper. In practice, these strategies are influenced by multiple factors, with the pressure differences, turbulence level, and thermal effects being most important. Therefore, the combined suppression parameter (CSP) on cavitation intensity has been introduced, as described in [67]. The concept of CSP also emphasizes that the temperature dependence cannot be omitted in the derivation of the theoretical function $M_L(t,T_r,v_r)$. One more aspect which should be mentioned is the geometry (or curvature) parameter [68]. On surfaces with a high curvature, the validity of the cavitation erosion tests can be somewhat decreased.

Based on the combined numerical and experimental modeling, it will be possible to predict changes in the three-dimensional shape of the eroded region in time approximately, as follows from Figure 16. These changes can modify the local flow field and the position of the most exposed regions. Consequently, changes in the wetted eroded surface should be periodically followed by the changes in the computational grids. Such a fluid–structure interaction will be a target of the authors' future work.

Author Contributions: Conceptualization, A.K. and M.S.; methodology, M.S. and A.K.; CFD, M.S.; validation, A.K. and M.K.; investigation, M.K. and M.F.; resources, A.K.; writing—original draft preparation, M.S.; writing—review and editing, M.S. and T.K.; visualization, M.S., T.K. and M.F.; project administration, T.K.; funding acquisition, T.K. All authors have read and agreed to the published version of the manuscript.

Funding: This research was funded by the Ministry of Industry and Trade of the Czech Republic, funding ID 28645413.

Data Availability Statement: The data presented in this study are available on request from the corresponding author. The data are not publicly available due to the huge size of datasets.

Acknowledgments: This research follows the results obtained in the projects MEYS CR: CZ.02.1.01/0.0/0.0/17_049/0008408 "Hydrodynamic Design of Pumps", and TACR: TN02000069/006 "Surfaces functionalization and postprocessing for industrial applications".

Conflicts of Interest: The authors declare no conflicts of interest.

References

1. Chahine, G.L.; Franc, J.P.; Karimi, A. Laboratory testing methods of cavitation erosion. Advanced Experimental and Numerical Techniques for Cavitation Erosion Prediction. In *Fluid Mechanics and Its Applications*; Kim, K.H., Chahine, G.L., Franc, J.P., Karimi, A., Eds.; Springer Science + Business Media: Dordrecht, The Netherlands, 2014; Volume 106, pp. 21–35. [CrossRef]
2. Steller, J.; Giren, B.G. *International Cavitation Erosion Test: Final Report*; Institute of Fluid-Flow Machinery of the Polish Academy of Sciences: Gdańsk, Poland, 2015.
3. Franc, J.P. Incubation time and cavitation erosion rate of work-hardening materials. *J. Fluid Eng.* **2009**, *131*, 021303. [CrossRef]
4. Franc, J.P.; Riondet, M.; Karimi, A.; Chahine, G.L. Impact load measurements in an erosive cavitating flow. *J. Fluid Eng.* **2011**, *133*, 121301. [CrossRef]
5. Zhang, J.; Richardson, M.O.W.; Wilcox, G.D.; Min, J.; Wang, X. Assessment of resistance of non-metallic coatings to silt abrasion and cavitation erosion in a rotating disk test rig. *Wear* **1996**, *194*, 149–155. [CrossRef]
6. Hong, S.; Wu, Y.; Wu, J.; Zheng, Y.; Zhang, Y.; Cheng, J.; Li, J.; Lin, J. Effect of flow velocity on cavitation erosion behavior of HVOF sprayed WC-10Ni and WC-20Cr3C2–7Ni coatings. *Int. J. Refract. Met. Hard Mater.* **2020**, *92*, 105330. [CrossRef]
7. Cheng, F.; Jiang, S.; Liang, J. Cavitation erosion resistance of microarc oxidation coating on aluminium alloy. *Appl. Surf. Sci.* **2013**, *280*, 287–296. [CrossRef]
8. Mochizuki, H.; Yokota, M.; Hattori, S. Effects of materials and solution temperatures on cavitation erosion of pure titanium and titanium alloy in seawater. *Wear* **2007**, *262*, 522–528. [CrossRef]
9. Usta, O.; Korkut, E. Prediction of cavitation development and cavitation erosion on hydrofoils and propellers by Detached Eddy Simulation. *Ocean Eng.* **2019**, *191*, 106512. [CrossRef]
10. Nohmi, M.; Ikohagi, T.; Iga, Y. Numerical prediction method of cavitation erosion. In Proceedings of the ASME-FEDSM, Jacksonville, FI, USA, 10–14 August 2008; Paper No: FEDSM2008-55126. [CrossRef]
11. Li, Z.; Pourquie, M.; Terwisga, T. Assessment of cavitation erosion with a URANS method. *J. Fluids Eng.* **2014**, *136*, 041101. [CrossRef]
12. Dular, M.; Stoffel, B.; Širok, B. Development of a cavitation erosion model. *Wear* **2006**, *261*, 642–655. [CrossRef]
13. Fortes-Patella, R.; Archer, A.; Flageul, C. Numerical and experimental investigations on cavitation erosion. *IOP Conf. Ser. Earth Environ. Sci.* **2012**, *15*, 022013. [CrossRef]
14. Huang, J.; Deng, L.; Ji, B.; Cheng, H. Comparative study of different cavitation erosion assessment methods in cavitating flow around a Delft twist hydrofoil. *IOP J. Phys. Conf. Ser.* **2024**, *2707*, 012133. [CrossRef]
15. Foeth, E.J.; Doorne, C.W.H.; Terwisga, T.; Wieneke, B. Time resolved PIV and flow visualization of 3D sheet cavitation. *Exp. Fluids* **2006**, *40*, 503–513. [CrossRef]
16. Lei, T.; Cheng, H.; Ji, B.; Peng, X. Numerical assessment of the erosion risk for cavitating twisted hydrofoil by three methods. *J. Hydrodyn.* **2021**, *33*, 698–711. [CrossRef]
17. Melissaris, T.; Bulten, N.; Terwisga, T. On the applicability of cavitation erosion risk models with a URANS solver. *J. Fluids Eng.* **2019**, *141*, 101104. [CrossRef]
18. Geng, L.; Zhang, D.; Chen, J.; Torre, O.; Escaler, X. Prediction of cavitation erosion with different erosion risk indicators. *Ocean Eng.* **2022**, *247*, 110633. [CrossRef]
19. Zhang, S.; Qian, Z.; Ji, B. Estimation of cavitation erosion area in unsteady cavitating flows using a modified approach. *Ocean Eng.* **2022**, *262*, 112229. [CrossRef]
20. Kevorkijan, L.; Pozdevsek, M.; Bilus, I.; Hren, G. Cavitation erosion modelling—Comparison of different driving pressure approaches. *Int. J. Simul. Model.* **2023**, *22*, 233–244. [CrossRef]
21. He, P.; Li, Z.; Liu, Q.; Zhang, X.; He, W. Prediction of cavitation dynamics and cavitation erosion around a three-dimensional twisted hydrofoil with an LES method. *Int. J. Nav. Archit. Ocean Eng.* **2023**, *15*, 100536. [CrossRef]
22. Zhu, H.; Qiu, N.; Wang, C.; Si, Q.; Wu, J.; Deng, F.; Liu, X. Prediction of cavitation evolution and cavitation erosion on centrifugal pump blades by the DCM-RNG method. *Hindawi Scanning* **2021**, *2*, 6498451. [CrossRef]
23. Koksal, C.S.; Usta, O.; Aktas, B.; Atlar, M.; Korkut, E. Numerical prediction of cavitation erosion to investigate the effect of wake on marine propellers. *Ocean Eng.* **2021**, *239*, 109820. [CrossRef]
24. Dular, M.; Coutier-Delgosha, O. Numerical modelling of cavitation erosion. *Int. J. Numer. Meth. Fluids* **2009**, *61*, 1388–1410. [CrossRef]
25. Peters, A.; Sagar, H.; Lantermann, U.; Moctar, O. Numerical modelling and prediction of cavitation erosion. *Wear* **2015**, *338-339*, 189–201. [CrossRef]
26. Peters, A.; Lantermann, U.; Moctar, O. Numerical prediction of cavitation erosion on a ship propeller in model- and full-scale. *Wear* **2018**, *408–409*, 1–12. [CrossRef]
27. Mohammadkhani, A.; Alizadeh, M. Numerical prediction of hydrodynamic cavitating flow structures and their corresponding erosion. *J. Hydrodyn.* **2021**, *33*, 546–571. [CrossRef]
28. Mo, X.; Wang, J.; Cheng, L.; Ouyang, T. Numerical prediction of vibration-induced cavitation erosion in high-speed gears using erosion risk indicators. *Tribol. Int.* **2023**, *179*, 108122. [CrossRef]
29. Farrell, K.J. Eulerian/Lagrangian analysis for the prediction of cavitation inception. In Proceedings of the CAV2001, Pasadena, CA, USA, 20–23 June 2001. A1.003.

30. Ochiai, N.; Nohmi, M.; Iga, Y.; Ikohagi, T. Numerical prediction of cavitation erosion in cavitating flows. In Proceedings of the CAV2009, Ann Arbor, MI, USA, 17–22 August 2009; p. 67.
31. Ochiai, N.; Iga, Y.; Nohmi, M.; Ikohagi, T. Numerical prediction of cavitation erosion intensity in cavitating flows around a Clark Y 11.7% Hydrofoil. *J. Fluid Sci. Technol.* **2010**, *5*, 416–431. [CrossRef]
32. Keller, J.B.; Kolodner, I.I. Damping of underwater explosion bubble oscillations. *J. Appl. Physics* **1956**, *27*, 1152–1161. [CrossRef]
33. Ochiai, N.; Iga, Y.; Nohmi, M.; Ikohagi, T. Study of quantitative numerical prediction of cavitation erosion in cavitating flow. *J. Fluids Eng.* **2013**, *135*, 011302. [CrossRef]
34. Eskilsson, C.; Bensow, R.E. Estimation of Cavitation Erosion Intensity Using CFD: Numerical Comparison of Three Different Methods. In Proceedings of the 4th International Symposiums on Marine Propulsors, Austin, TX, USA, 31 May–4 June 2015.
35. Sedlář, M.; Zima, P.; Komárek, M. Numerical prediction of erosive potential of unsteady cavitating flow around hydrofoil. *Appl. Mech. Mater.* **2014**, *565*, 156–163. [CrossRef]
36. Li, L.; Pei, C.; Wang, Z.; Lin, Z.; Li, X.; Zhu, Z. Assessment of cavitation erosion risk by Eulerian—Lagrangian multiscale modeling. *Int. J. Mech. Sci.* **2024**, *262*, 108735. [CrossRef]
37. Wang, Z.; Cheng, H.; Ji, B. Numerical prediction of cavitation erosion risk in an axisymmetric nozzle using a multi-scale approach. *Phys. Fluids* **2022**, *34*, 062112. [CrossRef]
38. Wang, Z.; Cheng, H.; Bensow, R.E.; Peng, X.; Ji, B. Numerical assessment of cavitation erosion risk on the Delft twisted hydrofoil using a hybrid Eulerian-Lagrangian strategy. *Int. J. Mech. Sci.* **2023**, *259*, 108618. [CrossRef]
39. Wang, Z.; Cheng, H.; Ji, B.; Peng, X. Numerical investigation of inner structure and its formation mechanism of cloud cavitating flow. *Int. J. Multiph. Flow* **2023**, *165*, 104484. [CrossRef]
40. Peters, A.; Moctar, O. Numerical assessment of cavitation-induced erosion using a multi-scale Euler-Lagrange method. *J. Fluid Mech.* **2020**, *894*, A19. [CrossRef]
41. Ji, B.; Wang, Z.; Cheng, H.; Bensow, R.E. Cavitation research with computational fluid dynamics: From Euler-Euler to Euler-Lagrange approach. *J. Hydrodyn.* **2024**, *36*, 1–23. [CrossRef]
42. Mihatsch, M.S.; Schmidt, S.J.; Thalhamer, M.; Adams, N.A. Numerical prediction of erosive collapse events in unsteady compressible cavitating flows. In Proceedings of the MARINE 2011, Lisbon, Portugal, 28–30 September 2011; pp. 499–510. [CrossRef]
43. Mihatsch, M.S.; Schmidt, S.J.; Adams, N.A. Cavitation erosion prediction based on analysis of flow dynamics and impact load spectra. *Phys. Fluids* **2015**, *27*, 103302. [CrossRef]
44. Blume, M.; Skoda, R. 3D flow simulation of a circular leading edge hydrofoil and assessment of cavitation erosion by the statistical evaluation of void collapses and cavitation structures. *Wear* **2019**, *428–429*, 457–469. [CrossRef]
45. Arabnejad, M.H.; Amini, A.; Farhat, M.; Bensow, R.E. Hydrodynamic mechanisms of aggressive collapse events in leading edge cavitation. *J. Hydrodyn.* **2020**, *32*, 6–19. [CrossRef]
46. Trummler, T.; Schmidt, S.J.; Adams, N.A. Numerical prediction of erosion due to a cavitating jet. *Wear* **2022**, *498–499*, 204304. [CrossRef]
47. Wang, Y.C.; Brennen, C.E. Numerical computation of shock waves in a spherical cloud of cavitation bubbles. *J. Fluids Eng.* **1999**, *121*, 872–880. [CrossRef]
48. ANSYS, Inc. *ANSYS CFX-Solver Theory Guide Release 2020 R2*; ANSYS, Inc.: Canonsburg, PA, USA, 2020.
49. Sedlář, M.; Krátký, T.; Komárek, M.; Vyroubal, M. Numerical analysis and experimental investigation of cavitating flows considering thermal and compressibility effects. *Energies* **2022**, *15*, 6503. [CrossRef]
50. Menter, F.R.; Egorov, Y. A scale-adaptive simulation model using two-equation models. In Proceedings of the 43rd AIAA Aerospace Sciences Meeting and Exhibition, Reno, Nevada, USA, 10–13 January 2005; p. 1095. [CrossRef]
51. Menter, F.R. Two-equation eddy-viscosity turbulence models for engineering applications. *AIAA J.* **1994**, *32*, 1598–1605. [CrossRef]
52. Hirt, C.W.; Nichols, B.D. Volume of fluid (VOF) method for the dynamics of free boundaries. *J. Comput. Phys.* **1981**, *39*, 201–225. [CrossRef]
53. Zwart, P.J.; Gerber, A.G.; Belamri, T. A Two-Phase Flow Model for Predicting Cavitation Dynamics. In Proceedings of the International Conference on Multiphase Flow, Yokohama, Japan, 30 May–3 June 2004; p. 152.
54. Zima, P.; Sedlář, M.; Müller, M. Modelling collapse aggressiveness of cavitating bubbles in hydromachinery. In Proceedings of the CAV2009, Ann Arbor, MI, USA, 17–22 August 2009.
55. Brennen, C.E. Fission of collapsing cavitation bubbles. *J. Fluid Mech.* **2002**, *472*, 153–166. [CrossRef]
56. Delale, C.F.; Pasinlioglu, S.; Zima, P. A criterion for the occurrence of bubble fission and its modeling. In Proceedings of the CAV2012, Singapore, 14–16 August 2012; p. 192. [CrossRef]
57. Zima, P.; Sedlář, M. Modeling bubble collapse aggressiveness in traveling bubble cavitation using bubble breakup model. In Proceedings of the CAV2012, Singapore, 14–16 August 2012; p. 209. [CrossRef]
58. Vogel, A.; Busch, S.; Parlitz, U. Shock wave emission and cavitation bubble generation by picosecond and nanosecond optical breakdown in water. *J. Acoust. Soc. Am.* **1996**, *100*, 148–165. [CrossRef]
59. Wang, Y.C. Effects of nuclei size distribution on the dynamics of a spherical cloud of cavitation bubbles. *J. Fluids Eng.* **1999**, *121*, 881–886. [CrossRef]
60. Kato, H.; Yamaguchi, H.; Maeda, M.; Kawanami, Y.; Nakasumi, S. Laser Holographic Observation of Cavitation Cloud on a Foil Section. *J. Vis.* **1999**, *2*, 37–50. [CrossRef]

61. Liu, Z.; Brennen, C.E. Cavitation nuclei population and events. *J. Fluid Eng.* **1998**, *120*, 728–737. [CrossRef]
62. Reuter, F.; Lesnik, S.; Ayaz-Bustami, K.; Brennen, G.; Mettin, R. Bubble size measurements in different acoustic cavitation structures: Filaments, clusters, and the acoustically cavitated jet. *Ultras. Sonochem.* **2019**, *55*, 383–394. [CrossRef]
63. Zhu, B.; Wang, H. Numerical prediction of impact force in cavitating flows. *IOP Conf. Ser. Earth Env. Sci.* **2010**, *12*, 012082. [CrossRef]
64. Sedlář, M.; Komárek, M.; Vyroubal, M.; Müller, M. Experimental and numerical analysis of cavitating flow around a hydrofoil. *EPJ Web Conf.* **2012**, *25*, 01084. [CrossRef]
65. Chahine, G.L.; Kalumuck, K.M. Development of a near real-time instrument for nuclei measurement: The ABS Acoustic Bubble Spectrometer. In Proceedings of the International Symposium Cavitation Inception, 4th ASME/JSME Joint Fluids Engineering Conference, Honolulu, HI, USA, 6–10 July 2003; FEDSM2003-45310. [CrossRef]
66. Thon-That, L. Experimental comparison of cavitation erosion rates of different steels used in hydraulic turbines. *IOP Conf. Ser. Earth Environ. Sci.* **2010**, *12*, 012052. [CrossRef]
67. Ge, M.; Sun, C.; Zhang, G.; Coutier-Delgosha, O.; Fan, D. Combined suppression effects on hydrodynamic cavitation performance in Venturi-type reactor for process intensification. *Ultrason. Sonochem.* **2022**, *86*, 106035. [CrossRef] [PubMed]
68. Wang, J.; Wang, Z.; Xu, Y.; Liu, H.; Yan, Y.; Zhang, J.; Li, S.; Ge, M. Analysis of the flow field characterization on the cavitation water jet applied to planar and curved surfaces. *Phys. Fluids* **2024**, *36*, 105172. [CrossRef]

Disclaimer/Publisher's Note: The statements, opinions and data contained in all publications are solely those of the individual author(s) and contributor(s) and not of MDPI and/or the editor(s). MDPI and/or the editor(s) disclaim responsibility for any injury to people or property resulting from any ideas, methods, instructions or products referred to in the content.